frontiers
in Astronomy and
Space Sciences

TYPE Original Research
PUBLISHED 16 October 2026
DOI 10.3389/fspas.2026.1909950

Check for updates

OPEN ACCESS

EDITED BY
Nithin Sivadas,
National Aeronautics and Space Administration, United States

REVIEWED BY
Roman Kislov,
Institute of Terrestrial Magnetism Ionosphere and Radio Wave Propagation (RAS), Russia
Harsha Gurram,
University of Maryland, United States

*CORRESPONDENCE
Dibyendu Nandy,
dnandi@rri.res.in

RECEIVED 15 June 2026
REVISED 05 September 2026
ACCEPTED 09 September 2026
PUBLISHED 16 October 2026

CITATION
Gupta S, Basak A and Nandy D (2026) Stellar wind driven Alfvén wing dynamics in planetary and exoplanetary magnetospheres.
Front. Astron. Space Sci. 13:1909950.
doi: 10.3389/fspas.2026.1909950

COPYRIGHT
© 2026 Gupta, Basak and Nandy. This is an open-access article distributed under the terms of the Creative Commons Attribution License (CC BY). The use, distribution or reproduction in other forums is permitted, provided the original author(s) and the copyright owner(s) are credited and that the original publication in this journal is cited, in accordance with accepted academic practice. No use, distribution or reproduction is permitted which does not comply with these terms.

Stellar wind driven Alfvén wing dynamics in planetary and exoplanetary magnetospheres

Sakshi Gupta[1,2,3], Arnab Basak[1,4] and Dibyendu Nandy[1,2,5]*

[1]Center of Excellence in Space Sciences India, Indian Institute of Science Education and Research Kolkata, Mohanpur, India, [2]Department of Physical Sciences, Indian Institute of Science Education and Research Kolkata, Mohanpur, India, [3]Center for High Energy Systems and Sciences, Defence Research and Development Organization, Hyderabad, India, [4]Department of Physics, Fakir Chand College, Diamond Harbour, India, [5]Raman Research Institute, Bengaluru, Karnataka, India

Magnetized obstacles embedded within a plasma flow generate magnetohydrodynamic structures known as Alfvén wings, which act as primary conduits for the transfer of momentum and energy between the body and the surrounding medium. This study employs three-dimensional resistive magnetohydrodynamic simulations to explore how these wings and the magnetosphere respond to diverse stellar wind conditions. Our results, gleaned from a large number of simulations spanning a wide range of stellar wind speed and magnetic field–and planetary dipole field–show that the global magnetospheric configuration is highly sensitive to the upstream Alfvén Mach number. We find that increasing stellar wind speed leads to a systematic closure and narrowing of Alfvén wing structures, while stronger stellar magnetic fields facilitate their opening. Analysis of the Alfvén wing morphology demonstrates a distinct dependence of wing opening angle on stellar wind speed, with internal wing analysis showing a reduction in plasma velocity and significant magnetic-flux accumulation. Our results exhibit a clear interdependence between the day-side magnetopause stand-off distance and the night-side magnetotail current sheet length. We find a linear scaling between the magnetotail dynamics and upstream forcing parameters. This study bridges the gap between solar system observations and (exo)planetary systems by demonstrating how Earth-like magnetospheres might transform into wing-dominated configurations during extreme stellar events or within the sub-Alfvénic regimes of close-in (exo)planets. Our findings can aid the interpretation of Alfvén wing signatures in observational data and enhance our understanding of how (exo)planetary magnetospheres respond to dynamic stellar wind forcing.

KEYWORDS
(exo)planetary magnetospheric dynamics, Alfvén wing, magnetohydrodynamics, planetary magnetosphere, star-planet interaction, stellar winds

1 Introduction

Alfvén wings are extended magnetohydrodynamic structures that can develop when a conducting planetary obstacle interacts with a magnetized plasma flow (Drell et al., 1965; Neubauer, 1980). The interaction perturbs the plasma velocity and ambient magnetic field, generating Alfvénic disturbances that propagate along the magnetic field while being advected by the plasma (Chané et al., 2012). Their formation can be understood by comparing the flow-advection timescale, $\tau_{\text{flow}} \approx L/V$, with the Alfvén-propagation timescale,

$\tau_A \approx L/V_A$, where L is a characteristic length scale of the interaction region. When $\tau_A < \tau_{\text{flow}}$, or equivalently when the local Alfvén Mach number $M_A = V/V_A < 1$, the disturbance propagates along the magnetic field faster than it is carried downstream by the plasma flow (Ridley, 2007). The combination of Alfvénic propagation and plasma advection produces two stationary, wing-like structures that facilitate the transfer of energy and momentum between the planetary obstacle and the surrounding plasma (Neubauer, 1980; Saur, J. et al., 2013).

In-situ observations have confirmed the formation of Alfvén wings at Earth during sub-Alfvénic intervals—the May 2002 event (Chané et al., 2012) and the April 2023 coronal-mass-ejection event (Chen et al., 2024) — when the passage of a coronal mass ejections (CME) driven magnetic cloud imposed sub-Alfvénic conditions ($M_A < 1$) on Earth's magnetosphere. Under such conditions, our planet can undergo a large magnetospheric transformation; global MHD simulations further confirm the associated reconnection and field-aligned current structures under sustained sub- Alfvénic driving (Ridley, 2007; Burkholder et al., 2024). Such conditions are expected to be routine for (exo)planets orbiting magnetically active stars or for the close-in (exo)planets. Magnetospheres act as dynamic shields that regulate how stellar winds interact with planets, controlling the transfer of energy, mass, and momentum between the star and the planetary environment. Rather than being static cavities, magnetospheres continually expand or contract in response to variations in stellar wind dynamic pressure. Depending on orbital distance, planetary and stellar wind properties, planets can experience very different wind regimes, which in turn lead to distinct magnetospheric configurations, i.e., variations in magnetopause standoff distance, bow-shock structure, and magnetotail dynamics (Lammer et al., 2007; Vidotto et al., 2014; Cohen et al., 2014; Basak and Nandy, 2021; Gupta et al., 2023).

The Alfvén Mach number M_A, defined as the ratio of the plasma flow speed to the local Alfvén speed, is a fundamental parameter controlling plasma behavior in magnetized environments. At Earth, the solar wind is typically strongly super-Alfvénic, with an Alfvén Mach number M_A of values around 5–8, indicating that the flow speed greatly exceeds the Alfvén speed. The value of M_A depends on the prevailing solar-wind conditions and on heliocentric distance (Zank et al., 2014). During transient solar events such as CMEs, M_A can drop significantly, altering the interaction with planetary magnetospheres (Ridley, 2007; Burkholder et al., 2024). In this work we do not model a specific heliocentric distance; instead, we prescribe the upstream stellar-wind conditions and examine the magnetospheric response across a wide range of M_A. We emphasise that, in all simulations presented here, the *upstream* flow remains super-Alfvénic ($M_A > 1$); the Alfvén-wing structures arise because the flow decelerates and the magnetic field piles up as the plasma approaches the planetary obstacle, so that the *local* Alfvén Mach number falls below unity in the near-planet wake. It is within these locally sub-Alfvénic regions that the wings develop.

Stellar wind parameters such as speed and magnetic field strength are highly variable across stellar types and evolutionary stages, with young, magnetically active stars producing winds that can be orders of magnitude denser and more magnetized than the present-day solar wind at Earth (Nandy and Martens, 2007; Vidotto et al., 2014; Vidotto and Cleary, 2020). These conditions are especially relevant for close-in exoplanets, which can frequently encounter sub- or near-Alfvénic stellar winds (Cohen et al., 2014). Highly active M dwarfs and young solar analogues can expose their planets to sustained intervals of low M_A, reshaping planetary magnetospheres and modulating star-planet interactions (See et al., 2014; Garraffo et al., 2017; Airapetian et al., 2020). Understanding how planetary magnetospheres respond under low and variable Alfvén Mach number regimes is therefore critical for interpreting planetary magnetospheric dynamics, assessing space weather phenomena and predicting electromagnetic signatures across diverse stellar systems.

The physical properties and geometry of Alfvén wings have been described in the foundational studies of (Drell et al., 1965; Neubauer, 1980). These magnetohydrodynamic structures are associated with field-aligned currents that develop along perturbed magnetic field lines. Analytically, the wing opening angle is predicted to scale as $\theta_A = \arctan(1/M_A)$ for a point-source conducting obstacle in a uniform magnetized plasma flow (Neubauer, 1980; Saur, J. et al., 2013). Alfvén wings have been observed at solar system bodies including Io and Ganymede within Jupiter's magnetosphere (Kivelson et al., 1997; Jia et al., 2008), at Mercury during a sub-Alfvénic interplanetary CME event (Bowers et al., 2025; Sarantos and Slavin, 2009) and transiently at Earth during extreme solar events (Chané et al., 2012; Burkholder et al., 2024; Chen et al., 2024; Gurram et al., 2025; Beedle et al., 2024). Previous global MHD studies have established that the morphology and opening angle of Alfvén wings depend on the upstream stellar-wind velocity and magnetic-field strength (Ridley, 2007; Jia et al., 2008; Saur, J. et al., 2013; Corso and Lai, 2026). Building on these results, the present study systematically investigates the combined influence of the stellar-wind velocity (V_{sw}), stellar-wind magnetic-field strength (B_{sw}), and planetary magnetic-field strength (B_p) using three-dimensional global resistive-MHD simulations. By independently varying these parameters, we examine how the upstream stellar-wind conditions and the strength of the planetary magnetosphere together control the Alfvén-wing morphology, magnetopause standoff distance, and magnetotail current-sheet structure. We further quantify these dependencies by exploring the Alfvén-wing opening angle and magnetotail current-sheet length across the parameter space. Observational signatures of these wings can be helpful in analyzing the star-planet magnetic interaction (Nichols and Milan, 2016; Szalay et al., 2020; Pineda and Villadsen, 2023).

The magnetotail current sheet links dayside and nightside magnetospheric dynamics, and its structure directly reflects the upstream stellar wind conditions driving the system (Dungey, 1961; Slavin et al., 1985; Lockwood, 1995). Within the Dungey-cycle framework, dayside reconnection opens magnetic flux that is transported into the tail lobes and later closed by nightside reconnection, so that changes in stellar wind conditions simultaneously affect both the magnetopause standoff distance and the tail geometry (Dungey, 1961; Milan et al., 2021). Stronger driving produces a more stretched tail with a longer current sheet favoring enhanced reconnection and plasmoid release, while weaker driving allows a shorter, more dipolar configuration (Sergeev et al., 2012; Lugaz et al., 2016; Ganushkina et al., 2018). These relationships have been extended to exoplanetary magnetospheres through global MHD simulations exploring how stellar wind conditions influence

magnetopause standoff distances, bow-shock locations, and large-scale field topology (Arridge et al., 2009; Vidotto et al., 2014; Cohen et al., 2014; Carolan et al., 2019; Basak and Nandy, 2021; Gupta et al., 2023; Roy and Nandy, 2023) The degree to which Alfvén wing structures further influence atmospheric escape, ionospheric coupling, and long-term planetary habitability has also been explored for planets orbiting M-dwarf stars where extreme and sustained wind conditions are common (Cohen et al., 2014; Vidotto and Cleary, 2020; Pérez-Torres, M. et al., 2021; Presa et al., 2024).

Recent studies have discussed the formation and properties of exoplanetary magnetospheres and Alfvén-wing configurations under a variety of stellar-wind conditions using different theoretical and numerical approaches (Belenkaya et al., 2022; Gupta et al., 2023; Belenkaya et al., 2024; Belenkaya, 2025). These studies have demonstrated the importance of the stellar-wind regime, planetary magnetic-field strength, and properties of the ambient plasma in determining the structure of exoplanetary magnetospheres and the occurrence of Alfvén-wing configurations. The present study extends these investigations by employing three-dimensional resistive MHD simulations to systematically examine the coupled response of Alfvén-wing morphology and global magnetospheric structure to variations in stellar-wind speed, stellar-wind magnetic-field strength, and planetary dipole strength. We quantify the dependence of the wing opening angle on the upstream Alfvén mach number, examine the relationship between the dayside magnetopause stand-off distance and nightside magnetotail current-sheet length, and investigate the internal plasma and magnetic-field properties of the wings. We further identify an empirical scaling between the magnetotail current-sheet length and the composite upstream forcing parameter. Thus, rather than introducing the possibility of Alfvén-wing formation itself, which is well established, our aim is to provide a systematic characterization of the coupled wing–magnetosphere response across a broad range of stellar-wind and planetary magnetic-field conditions within a unified three-dimensional resistive-MHD framework.

In this work, we present 90 three-dimensional resistive MHD simulations spanning a wide parameter space of stellar wind speeds ($1-10\,v_{sw}$), stellar magnetic fields (10–50 nT), and planetary dipole strengths ($0.5-2\,B_e$). We systematically characterize the morphological evolution of Alfvén wings from broad, open structures at low M_A to collimated, flow-aligned geometries at high M_A, and validate the simulated wing opening angles with the analytical prediction of (Neubauer, 1980). We discuss the relationships linking magnetopause standoff distance to magnetotail current sheet length, analyze the internal velocity and magnetic-field structure within the wings, and identify the scaling between the composite upstream forcing parameter $\widetilde{\Pi} = (v_{sw}/v_0)^2/(B_{sw}/B_0)$ and the magnetotail current sheet length. These results provide a coherent framework for interpreting Alfvén wing signatures and magnetospheric response across both solar system and exoplanetary environments subject to diverse stellar wind forcing.

This paper begins with the model description in Section 2 in which we give an overview of the theory and numerical setup employed in this study. The detailed findings are presented in Section 3 followed by the conclusion in Section 4.

2 Model description

We adapt the Star-Planet Interaction Module (CESSI-SPIM) developed by Das et al. (2019), based on the PLUTO MHD solver (Mignone et al., 2007), to simulate different configurations of stellar winds and planetary magnetospheres. The governing resistive-MHD equations are given by Equations 1–4.

$$\partial_t \rho + \nabla \cdot (\rho \vec{v}) = 0 \tag{1}$$

$$\partial_t \vec{v} + (\vec{v} \cdot \nabla)\vec{v} + \frac{1}{4\pi\rho}\vec{B} \times \left(\nabla \times \vec{B}\right) + \frac{1}{\rho}\nabla P = \vec{g} \tag{2}$$

$$\partial_t E + \nabla \cdot \left[(E+P)\vec{v} - \vec{B}\left(\vec{v} \cdot \vec{B}\right) + \left(\eta \cdot \vec{J}\right) \times \vec{B}\right] = \rho \vec{v} \cdot \vec{g} \tag{3}$$

$$\partial_t \vec{B} + \nabla \times \left(\vec{B} \times \vec{v}\right) + \nabla \times \left(\eta \cdot \vec{J}\right) = 0 \tag{4}$$

where the symbols ρ, v, $\vec{B}$, P, E, η and $\vec{g}$ and denote density, velocity, magnetic field, pressure, total energy density, magnetic diffusivity and gravitational acceleration due to the planet respectively. The quantity $\vec{J}$ is the current density given by $\nabla \times \vec{B}$, ignoring the displacement current. Equation 5 defines the total energy density for an ideal-gas equation of state.

$$E = \frac{P}{\gamma - 1} + \frac{\rho v^2}{2} + \frac{B^2}{8\pi} \tag{5}$$

The computational domain extends from $-80\ R_p$ to $200\ R_p$ in the x-direction, $-45\ R_p$ to $45\ R_p$ in the y-direction and $-200\ R_p$ to $200\ R_p$ in the z-direction, where R_p is the radius of the planet which is located at the origin of the Cartesian box. Considering the constraints of our modest computational facility, a combination of stretched and uniform grid types is used in the x and z directions for all the simulations in this study. We adopt a similar simulation set-up as studied in Gupta et al. (2023), in which we explore the impact of changing stellar and planetary magnetic field strength on the planetary magnetosphere. For model description and grid resolution kindly refer to Gupta et al. (2023). We consider a finite and isotropic magnetic diffusivity η, as the causal mechanism for non-ideal processes such as magnetic reconnections. The magnetic diffusivity lies within the range of realistic values as shown in earlier studies (Raeder, 1999; Komar et al., 2013; Varela, J. et al., 2022).

In this study, an Earth-like planet is considered with similar mass, radius, and tilt while the stellar wind properties such as magnetic field and velocity are varied. While the setup uses Earth-like parameters (mass, radius, tilt) for the planet, the varying M_A allows these results to be scaled to different magnetized (exo)planets. We perform a comprehensive parameter-space study consisting of ninety independent three-dimensional simulations. These runs encompass all relevant combinations of the varying stellar wind speeds and magnetic fields as well as planetary dipole fields, allowing for a characterization of magnetospheric response across a wide parameter space and are necessary for understanding the interactions occurring in different exoplanetary systems.

We perform a set of simulations by using stellar wind speed values $\{1, 1.25, 1.5, 2, 2.5, 3, 3.5, 5, 8, 10\}\ v_0$, stellar wind magnetic field strength values $\{10, 30, 50\}$ nT and planetary dipole field strength values $\{0.5\ B_e,\ B_e,\ 2\ B_e\}$ with all possible combinations between them. Here $B_e = 3.1 \times 10^4$ nT denotes surface equatorial magnetic

field strength of the Earth's dipolar field and v_{sw} is the stellar wind speed. In the present study we assumes a southward-oriented IMF only, the future work will explore the impact of IMF orientation on the magnetospheric configurations.

The upstream Alfvén Mach number, $M_{A,\mathrm{up}}$, defined by Equation 6 is calculated for the different stellar-wind parameter combinations considered in this study.

$$M_{A,\mathrm{up}} = \frac{v_{sw}\sqrt{4\pi\rho_{sw}}}{B_{sw}}. \tag{6}$$

The upstream value should be distinguished from the local Alfvén Mach number, M_A, which varies throughout the simulation domain as the plasma velocity, density, and magnetic-field magnitude changes during the interaction with the planetary magnetosphere. The spatial distribution of the local Alfvén Mach number is shown in Figure 1B, where the $M_A = 1$ contour delineates the locally sub-Alfvénic regions associated with the Alfvén-wing structures.

We initialize a conducting plasma atmosphere surrounding the planet. The atmospheric density profile is defined by Equation 7

$$\rho_p = 10^6 \rho_{amb} \qquad r \le R_p$$

$$\rho_{atm}(r) = \rho_p + \frac{(\rho_{amb} - \rho_p)}{2}\left[\tanh\left\{9\left(\frac{r}{R_P} - 2\right)\right\} + 1\right] \qquad R_P \le r \le 3R_p \quad , \tag{7}$$

where ρ_p, ρ_{amb} and ρ_{atm} are the densities of the planet, ambient medium and atmosphere respectively and r is the radial distance from the origin. For more details on the justifications for the choice of the above atmospheric profile, please refer to Section 2.1 of Basak and Nandy (2021). The atmospheric pressure distribution is obtained by integrating the hydrostatic-balance relation given in Equation 8.

$$\frac{dP}{dr} = -\rho_{atm}(r)g(r) \tag{8}$$

Here, the gravitational field is given by $g(r) = -\frac{GM_p}{r^2}$ where M_p is the planetary mass. The pressure inside the planet is evaluated by extrapolating the value of pressure at the planet-ionosphere boundary. The density and pressure in the region $r > 3R_p$ is initialized to be equal to that in the ambient medium (Table 1).

The input parameters at the stellar wind injection boundary (at $x = -80\ R_p$ in the yz plane) are obtained by solving the Rankine-Hugoniot magnetized jump conditions for the given shock velocity. A southward oriented (SIMF) stellar wind is injected with density $\rho_{sw} = 4\ \rho_{amb}$. For all other faces of the Cartesian box, force-free outflow boundary condition is implemented. The parameters defining the properties of the stellar wind and planet are varied in each run and the steady state configuration of the planetary magnetosphere is analyzed.

3 Results and Discussions

The nature of interaction between the stellar wind and the planetary magnetosphere is governed by the combined effect of plasma flow speed, stellar and planetary magnetic field strengths, and the resulting Alfvén Mach number. Our three-dimensional magnetohydrodynamic (MHD) simulations explore how variations in stellar wind speed and magnetic field strength shape the global planetary magnetospheric configuration and topology, the Alfvén wing morphology, and associated current systems, especially in the night-side wake region. The results presented here provide insights into the formation and evolution of Alfvén wings, the impact on wing opening angle, and the properties of the magnetotail current sheet under dynamic stellar wind conditions.

As the stellar wind speed increases, the Alfvén Mach number also increases, thereby altering the spatial extent and geometry of Alfvén wings. These findings are directly relevant to solar system planets during extreme solar events and exoplanets orbiting active stars, where such wind conditions occur often (Ridley, 2007; Vidotto et al., 2014; Burkholder et al., 2024).

3.1 Morphological evolution of Alfvén wings with stellar wind speed

The Alfvén wing geometry in the night-side magnetotail region of the planetary magnetosphere changes considerably as the incoming stellar wind is varied from weak to strong flow conditions. Figure 1A illustrates the morphological evolution of the Alfvén wings in the planetary night-side magnetotail region as a function of the increasing stellar wind speed for fixed values of planetary and stellar wind magnetic fields. The top row [panels (a)–(c)] of Figure 1A corresponds to steady-state planetary magnetospheric configuration for stellar wind speed values v_0, 1.25 v_0 and 1.5 v_0 while the bottom row [panels (d)-(f)] shows the same for wind speeds 2 v_0, 5 v_0 and 10 v_0 respectively. The varying magnetospheric geometry with stellar wind speed as shown in the plots indicate that the ambient plasma flow strongly shapes the planetary environment. The configuration in Figure 1A provides an Earth-like reference but should not be regarded as an exact representation of the present-day Sun–Earth interaction. The incoming plasma in the upstream flow is decelerated and the magnetic field is compressed and draped as it approaches the planetary obstacle, resulting in a reduction of the local Alfvén Mach number. The local M_A distribution with $M_A < 1$ around the planetary obstacle extends downstream along the wing-like structures. The extent of this locally low-M_A region, and hence the morphology of the resulting structures, depends on both the upstream stellar-wind parameters and the planetary magnetic-field strength. When the stellar wind speed is gradually increased keeping other parameters fixed, the Alfvén wings tend to close down slowly which is evident from the decreasing wing opening angle. The corresponding spatial distributions of the local Alfvén Mach number are shown in Figure 1B. The yellow contour represents $M_A = 1$ and delineates the locally sub-Alfvénic regions, $M_A < 1$, that form around the planetary obstacle and extend downstream along the wing-like structures. Although the prescribed upstream conditions are characterized by a single upstream Alfvén Mach number, $M_{A,\mathrm{up}}$, the local value of M_A varies throughout the simulation domain because the plasma velocity, density, and magnetic-field changes during the interaction with the planetary magnetosphere. As the stellar-wind speed increases, the locally sub-Alfvénic regions become progressively narrower and diminish in spatial extent, consistent with the decreasing wing opening angle and

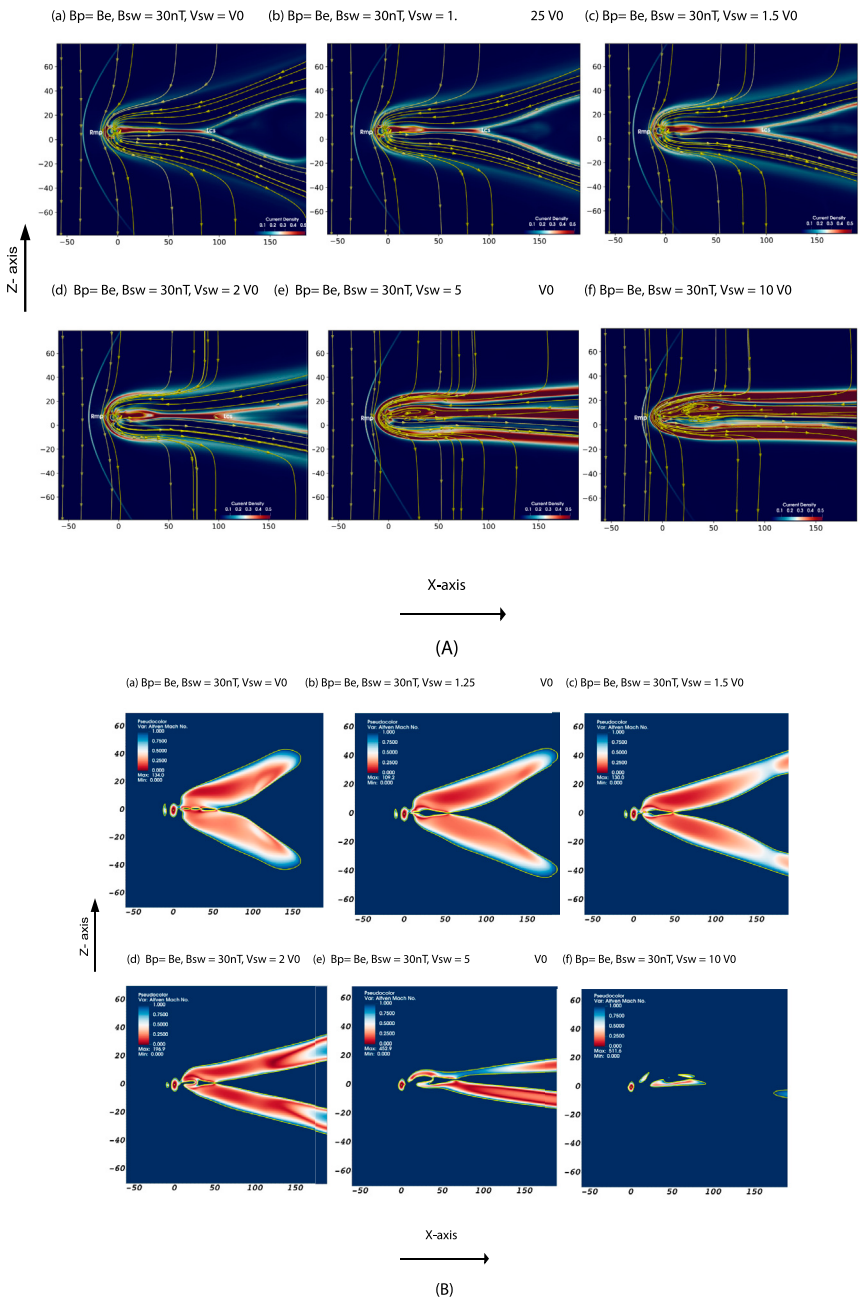


FIGURE 1
Steady-state planetary magnetospheric configurations for increasing stellar-wind speed, with $B_p = B_e$ and $B_{sw} = 30$ nT. Panels (a–f) correspond to v_0, $1.25v_0$, $1.5v_0$, $2v_0$, $5v_0$, and $10v_0$, respectively. The corresponding values of (R_{mp}/R_p, L_{cs}/R_p) for panels (a–d) are (7.60, 79.10), (7.31, 82.04), (6.69, 84.68), and (6.20, 93.78), respectively. For panels (e,f) R_{mp}/R_p is 5.35 and 5.20, respectively; L_{cs} is not reported because no distinct downstream bifurcation of the wing branches is identified in these cases. **(A)** Current-density magnitude in the $y = 0$ meridional plane, with magnetic-field lines and vectors indicating the field geometry and direction. **(B)** Corresponding local Alfvén Mach-number distributions. The yellow contour represents $M_A = 1$ and delineates the locally sub-Alfvénic regions, $M_A < 1$, associated with the Alfvén-wing structures.

the increasingly collimated, flow-aligned magnetotail configuration. At the lowest wind speed [Figure 1A panel (a)], broad and well-developed Alfvén wings extend above and below the ecliptic plane in the planetary night-side with a large opening angle forming two nearly symmetric current-carrying structures that connect the planetary obstacle to the ambient plasma. This configuration is characterized by strongly locally sub-Alfvénic interaction in a low plasma-β environment. Under these conditions—where both the local Alfvén mach number $M_A < 1$ and the plasma $\beta \ll 1$ — perturbations excited at the planet propagate preferentially along the magnetic field direction, efficiently channeling energy into the Alfvén wings and inflating them laterally. In the magnetotail region downstream of the planet, the magnetic pressure dominates over the thermal pressure, ensuring that the low-β condition is

TABLE 1 Values of physical parameters used in the simulations and their respective notations.

Physical quantity	Notation	Value used
Density in ambient medium	ρ_{amb}	1.5×10^{-23} g cm^{-3}
Pressure in ambient medium	P_{amb}	2.49×10^{-11} dyne cm^{-2}
Density of stellar wind	ρ_{sw}	$4\,\rho_{amb}$
Velocity of stellar wind	v_0	3.5×10^7 cm s^{-1}
Adiabatic index	γ	5/3
Planetary mass	M_p	5.972×10^{27} g
Planetary radius	R_p	6.371×10^8 cm
Intrinsic planetary magnetic field	B_p	$0.5B_e$, B_e and $2B_e$ *
Stellar wind magnetic field strength	$\lvert B_{sw}\rvert$	10 nT, 30 nT and 50 nT
Magnetic diffusivity	η	10^{13} cm^2 s^{-1}
Magnetospheric tilt angle	θ_p	11°

*The symbol B_e represents the magnetic field for the case of the Earth's dipole.

satisfied and the wing structure is maintained. For the highest wind speed however [Figure 1A panel (f)], the wings in the night-side cannot be distinguished separately since they come close together with negligible opening angle, straighten out and become almost parallel to the ecliptic plane. The plasma flow velocity is now strong enough to generate ample ram pressure that forces the wings down and aligns the extended magnetosphere along the flow direction. This increased ram pressure is also responsible for compressing the planetary field at the day-side leading to a lower magnetopause stand-off distance. The overall trend of the plots in the above figure reflects that as the Alfvén Mach number (M_A) increases, the ability of the plasma to communicate disturbances across field lines diminishes, confining Alfvénic perturbations more tightly to the direction of the flow. In our simulations, this progressive "closure" of the wings from wide open structures at low v_{sw} to more collimated, flow-aligned wings at higher v_{sw}, is evident across the panels (a)–(f). The results also reveal that the current density is highest along the wing boundaries, indicating that these structures are defined by intense field-aligned currents.

In order to provide a proper quantification of the morphological trends observed in Figure 1, we plot the Alfvén wing opening angle as a function of both stellar wind speed and magnetic field for three values of planetary dipole field. In Figure 2A, the panels (a), (b) and (c) correspond to a given planetary field strength, i.e., B_p = 0.5 B_e, B_e and 2 B_e respectively. In each panel, blue, green and red dots show the measured opening angles for simulation data with B_{sw} = 10 nT, 30 nT and 50 nT respectively as a function of v_{sw}. The corresponding smooth curves represent best fits to the simulation data. To quantify the opening angle of the Alfvén-wing structures, we use a geometrical construction based on three points in the meridional plane. The point P_0 is defined as the central point in the downstream magnetotail from which the current sheet bifurcates into the upper and lower branches. At a fixed downstream distance of $x = 120\,R_p$, points P_1 and P_2 are identified on the upper and lower branches, respectively. The opening angle is then defined as the angle subtended by these two branches at P_0, $\theta = \angle P_1P_0P_2$. It is calculated from the vectors $\mathbf{v}_1 = P_1 - P_0$ and $\mathbf{v}_2 = P_2 - P_0$ as

$$\theta = \arccos\left(\frac{\mathbf{v}_1 \cdot \mathbf{v}_2}{|\mathbf{v}_1|\,|\mathbf{v}_2|}\right). \tag{9}$$

Similarly, the opening angle is computed using Equation 9 for all the simulation cases shown in Figure 2 to quantify the dependence of the opening angle on the planetary magnetic-field strength. Let us first consider the scenario for a fixed planetary field. In any of the given panels in Figure 2A, it is observed that for slow winds, where the local interaction is strongly sub-Alfvénic, the wing opening angle is larger. A stronger planetary dipole creates a more "rigid" obstacle that resists the lateral inflation of the wings, forcing them to remain closer to the ecliptic plane. As v_{sw} is increased keeping B_{sw} constant, the wing opening angle gradually decreases which is the effect of the increasing ram pressure of the wind plasma that shuts the wings down and aligns them in its direction. As v_{sw} increases and the interaction becomes increasingly super-Alfvénic even locally, the wing opening angle reaches an asymptotic minimum–this indicates the extent up to which the wings may be closed for a given value of B_{sw}. The results depict a regime change where the kinetic energy of the wind completely dominates the magnetic tension of the wings, effectively 'pinching' the structures into a tail-like geometry.

Considering the influence of varying magnetic fields on the Alfvén wing topology as shown in Figure 2A we observe that for a given stellar wind speed v_{sw} and planetary dipole field B_p, as the stellar wind magnetic field strength B_{sw} is increased from 10 nT to 50 nT, the wing opening angle becomes larger for a higher value of B_{sw} in all three panels. A higher value of B_{sw} indicates a larger local Alfvén speed and the tendency for the local interaction to remain sub-Alfvénic over a wider region and a wider range of v_{sw}. A stronger stellar wind magnetic field pulls the wings outwards away from the ecliptic plane due to the existence of a stronger Lorentz force acting on the plasma field lines in the magnetotail region–this increases the wing opening angle. Conversely, increasing the planetary magnetic field across the three panels (Figures 2A–C) reduces the wing opening angle for fixed values of v_{sw} and B_{sw}. This implies that a stronger magnetic obstacle confines the wings more tightly around the magnetosphere and requires stronger wind forcing to open them to comparable extents. This occurs because the Lorentz force due to a stronger planetary field acts in a direction opposite to that due to the stellar magnetic field and tends to close the wings down. It is pertinent to mention here that in Figures 2A,C, we show the wing opening angle only for stellar wind magnetic field B_{sw} = 30 nT and 50 nT because for the case B_{sw} = 10 nT, the Alfvén wings do not open sufficiently due to a very strong planetary field as compared to the stellar wind magnetic field and therefore, the wing opening angle is negligible for this case.

To validate the Alfvén wing physics captured by our simulations, we compare the measured wing opening angles with the analytical prediction of Neubauer (1980), $\theta_A = \arctan(1/M_A)$, which assumes a point-source conducting obstacle in a uniform magnetized plasma flow. Figure 2B shows the simulated opening angles ($\theta_{\rm sim}$) plotted against the corresponding Neubauer predictions ($\theta_{\rm Neubauer}$) for all parameter combinations across the three planetary dipole strengths. The data follow a clear positive correlation with the analytical values across all panels, confirming that the Alfvén Mach number is the primary controlling parameter

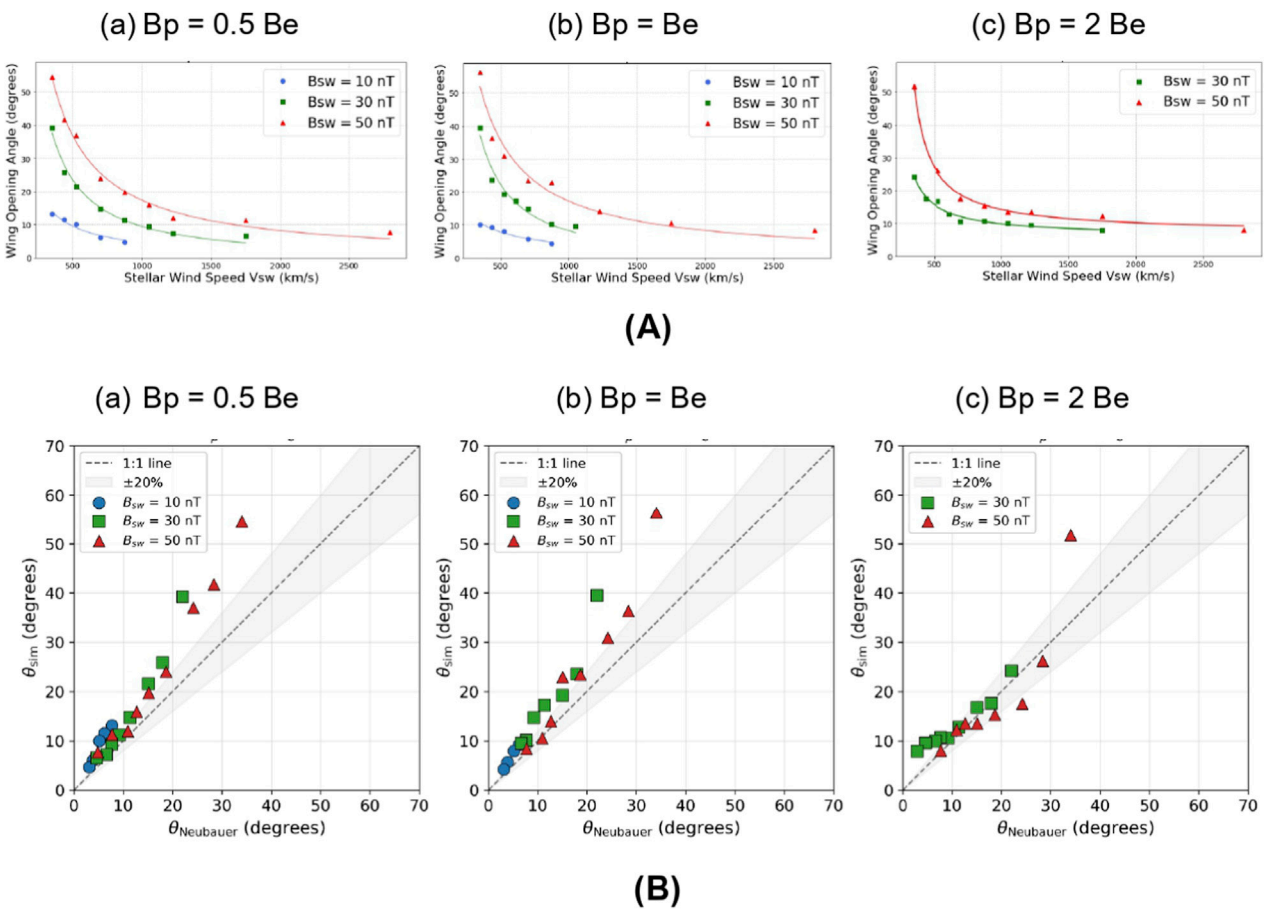


FIGURE 2
(A) Plots of the night-side Alfvén wing opening angle as a function of stellar wind speed for different stellar and planetary magnetic field strengths. Panels (a-c) correspond to planetary dipole field strengths of 0.5 B_e, 1.0 B_e, and 2.0 B_e respectively. In each panel, the blue, green, and red data points correspond to B_{sw} = 10, 30, and 50 nT, respectively. While the solid curves show the corresponding best-fit trends to these simulation data. **(B)** Comparison of simulated Alfvén wing opening angles (θ_{sim}) with the analytical prediction of (Neubauer, 1980), $\theta_{Neubauer} = \arctan(1/M_A)$. The dashed line indicates perfect agreement and the shaded band marks ±20% deviation. The plots illustrate that for a fixed planetary field, the Alfvén wings open up for a higher stellar wind magnetic field due to a stronger force acting in the magnetotail region. However, when the planetary field strength is increased, it opposes this force and tends to close the wings down again. The interplay between stellar and planetary magnetic fields in addition to stellar wind speed is responsible for the Alfvén wing geometry and the steady-state magnetospheric topology.

for the wing geometry. Few data points for the simulated angles exceed the Neubauer prediction with data points lying above the 1:1 line. This departure arises because the Neubauer formulation treats the obstacle as a point conductor with zero spatial extent, whereas in our simulations the planetary magnetosphere acts as a finite, inflated obstacle that deflects the incoming stellar wind over a cross-section significantly larger than the planetary radius. This effectively broadens the interaction region and leads to the formation of the wing current sheets at larger angular separations than predicted by the point-source model.

The above results provide a comprehensive characterization of Alfvén wing geometry across the three-dimensional parameter space of stellar wind speed, stellar magnetic field, and planetary dipole strength. The validated agreement with the Neubauer (1980), along with the quantified departures arising from finite magnetospheric effects, provides a foundation for interpreting observed wing signatures to underlying stellar wind conditions in both the solar system and (exo)planetary environments.

3.2 Magnetotail current sheet response to magnetopause variability

The response of the planetary magnetotail to changing stellar wind conditions is closely related to the behavior of the day-side magnetopause. We have seen that an increase in stellar wind ram pressure compresses the day-side magnetopause and alters the global magnetospheric configuration, the geometry of the Alfvén wings and the structure of the magnetotail current sheet. In order to quantify this relationship, we analyze the night-side magnetotail current sheet length (L_{cs}) variation as a function of the day-side magnetopause stand-off distance (R_{mp}) for a range of stellar wind speeds and magnetic field strengths for different planetary dipole field strengths. For studying the night-side response, we define the magnetotail current sheet length (L_{cs}) as the distance

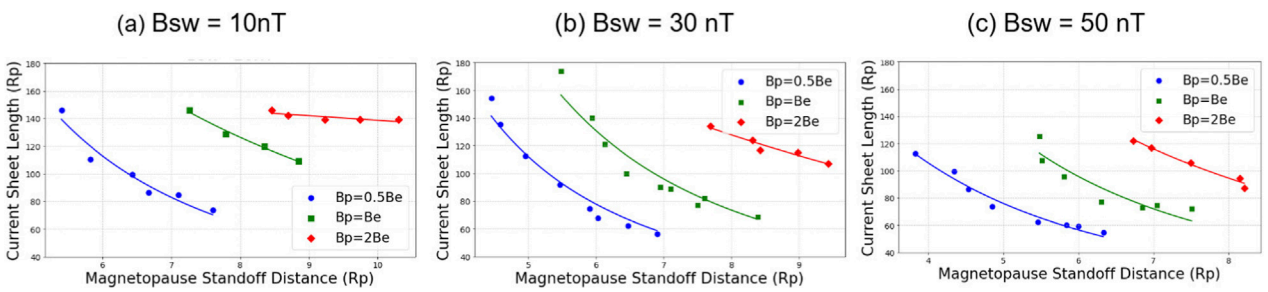


FIGURE 3
Relationship between the night-side magnetotail current sheet length and the subsolar magnetopause standoff distance for different planetary and stellar wind magnetic field strengths. Panels **(a-c)** correspond to stellar wind magnetic field 10 nT, 30 nT and 50 nT respectively. In each panel, data points in blue, green and red colors correspond to planetary dipole strengths of 0.5 B_e, 1.0 B_e, and 2.0 B_e respectively while the solid curves show the corresponding best-fit to the simulation data. As expected, the night-side current sheet length and the day-side magnetopause stand-off distance show an inverse relation between them for fixed parameter values. Increasing the planetary field keeping stellar field constant increases the values of both current sheet length and magnetopause stand-off distance while increasing the stellar field keeping planetary field constant lowers their values.

from the planet to the point where the current sheet begins to bifurcate in the magnetotail wake region. The magnetotail current sheet remains a single structure in the near-planetary wake and bifurcates farther downstream into two branches. The location of this bifurcation varies with the stellar-wind and planetary magnetic-field strengths, as shown in Figures 3, 4. For details on the identification of the bifurcation region and the computation of current sheet length, kindly refer the Results and Discussion section of (Gupta et al., 2023).

Figure 3 shows the variation of magnetotail current sheet length with day-side magnetopause stand-off distance R_{mp} for three values of stellar wind magnetic field B_{sw} = 10 nT, 30 nT and 50 nT in panels (a), (b) and (c) respectively. In each panel, the simulation data points and their corresponding best-fit curves are shown for planetary magnetic field strengths $B_p = 0.5B_e$, $B_p = B_e$, and $B_p = 2B_e$ in blue, green and red colors respectively. The data points for any given curve are obtained by varying the stellar wind speed and measuring the corresponding magnetopause stand-off distance and magnetotail current sheet length for a particular wind speed. We first consider a single case, for instance the blue curve in panel (a), for understanding the trend of the results so obtained. The following explanation however holds for any given case in the present figure. The data exhibit a clear inverse relationship between magnetopause stand-off distance and the current sheet length, well captured by the fitted curves (see Figure 3). As R_{mp} increases, the magnetotail current sheet becomes shorter and vice-versa. When the stellar wind speed is lower, the ram pressure is also less and so is the day-side magnetospheric compression which leads to a larger magnetopause stand-off distance. When the wind speed is gradually increased, the ram pressure increases which compresses the day-side magnetosphere even more and lowers the value of the stand-off distance. The higher wind speed advects the night-side magnetotail and stretches it further along its direction which results in a longer current sheet in the wake region. This indicates that as the wind speed increases, the day-side penetration is higher resulting in a lower stand-off distance while the night-side advection leads to a longer current sheet. This behavior reflects the response of the magnetosphere to enhanced stellar wind forcing where the day-side and night-side properties are inversely related to each other. The elongation of the current sheet observed here is intrinsically linked to the 'closure' of the Alfvén wings discussed in Section 3.1 – as the wings align more closely with the flow, the magnetosphere is transformed into a more stretched, tail-dominated geometry.

Now, let us consider any of the three panels in Figure 3 for understanding the impact of varying planetary magnetic field on the magnetospheric topology. We find that as the planetary field is increased (from blue to red via green), the curves are shifted to larger values of both day-side stand-off distance and night-side current sheet length. For a stronger planetary magnetic field, the day-side magnetic pressure close to the planet is higher which nullifies the stellar wind ram pressure further away from the planetary surface resulting in a larger value of magnetopause stand-off distance. A stronger intrinsic dipole field increases the internal magnetic pressure which effectively 'inflates' the entire magnetospheric cavity. We have already seen in Figure 2 that a stronger planetary magnetic field tends to close the Alfvén wings down in the magnetotail region as evident from the decreasing wing opening angle. The more the wings come together, the longer is the magnetotail current sheet due to oppositely directed magnetic field lines in the upper and lower halves of the ecliptic plane. Therefore, a stronger planetary field results in a longer night-side current sheet.

For understanding the impact of varying stellar wind magnetic field on the magnetospheric structure, let us move across the panels from left to right in Figure 3 for increasing B_{sw}. When the stellar wind magnetic field is low, magnetic reconnections at the planetary day-side are less which leads to a larger magnetopause stand-off distance. When the stellar magnetic field considered in this study is increased, the reconnection rate increases and the stellar penetration is more into the planetary magnetosphere thereby decreasing the stand-off distance. For understanding the dynamics in the night-side, we again refer to Figure 2 where it is found that a stronger stellar field pulls the Alfvén wings apart due to higher magnetic tension as depicted by the larger wing opening angle–this geometry ensures that only a small portion of the oppositely directed field lines are close to each other near the ecliptic plane and this leads to a shorter magnetotail current sheet. This suggests that a strongly magnetized stellar wind acts as a confining sheath that limits the expansion of the magnetotail regardless of the day-side compression state.

This inverse relationship is consistently observed across all stellar magnetic field cases shown in Figures 3A–C, indicating

that the coupled dayside–nightside response is robust across the explored parameter space. Summarizing the impact of varying stellar wind speed and stellar and planetary magnetic fields on the magnetospheric geometry, we note that a higher v_{sw} compresses the magnetosphere on the day-side and elongates it on the night-side, a stronger B_{sw} increases magnetic confinement, leading to a more compact magnetosphere and shorter magnetotail current sheet, and a stronger B_p leads to a more extended magnetosphere in both directions.

3.3 Properties of plasma flow and magnetic field inside the Alfvén wings

For understanding the stellar wind crafted planetary environment for different parameter values, we analyze the local plasma properties along the z-axis in the in the y = 0 meridional plane at a fixed downstream location x = 100 R_p in the night-side magnetotail. A fixed downstream location of x = 100 R_p is selected for the 1D cuts to provide a common diagnostic plane within the developed Alfvén-wing region across all simulation cases. This location is chosen for consistency of comparison. The qualitative trends in the plasma flow and magnetic-field properties remain unchanged for cuts taken at other locations within the developed wing region, although their magnitudes may vary.

Figure 5A depicts the variation of plasma velocity (v_{mag}) as a function of the distance along z-axis from $-80R_p$ to $80R_p$ for $B_p = B_e$ and three different stellar wind speeds (v_0, 2 v_0 and 5 v_0) shown in blue, green and red colors respectively. The stellar wind magnetic field strength increases across the panels (a)-(c) from 10 nT to 50 nT. In all cases, there is a marked reduction in flow speed within the wings compared to the ambient medium, i.e., the flow decelerates inside the Alfvén wings. If we move across panels (a)-(c) in Figure 5A, the lateral extent of the Alfvén wings increases with stellar wind magnetic field strength whereas for any fixed combination of planetary and stellar magnetic fields, the wings become narrower when the stellar wind speed is higher. The red curves ($5v_0$) show the most prominent drop in velocity. This suggests that as the stellar wind speed increases, the Alfvén wings become regions of intense drag, where a larger fraction of the wind's kinetic energy is converted into magnetic energy (and potentially thermal energy through dissipation processes), leading to enhanced magnetic pressure within the wings.

The corresponding magnetic field magnitude profiles are plotted in Figure 5B along the same route. The plots show that the field strength inside the wings is consistently higher than the background ambient magnetic field. This "pile-up" of magnetic field occurs due to the clustering of planetary magnetic field lines reconnected with the stellar field in both the upper and lower parts of the magnetotail. The orientation of these two structures however depends on the parameter values, i.e., stellar wind speed and stellar and planetary magnetic fields. The enhanced magnetic pressure within the wings opposes the incoming plasma flow, leading to a significant reduction in velocity. For all three panels (a)-(c) in Figure 5B, it is evident that higher incoming stellar wind speeds are associated with larger magnetic field magnitudes inside the wings, implying that faster flows advect the magnetotail and compress the magnetic flux more. In addition, when the stellar wind magnetic field is increased, the regions of enhanced magnetic field broaden, indicating that stronger upstream fields produce wider Alfvén wings.

These results demonstrate that Alfvén wings are not merely geometric structures but regions of significant dynamical interaction, where plasma flow is slowed and magnetic flux is enhanced. These dynamics plays a key role in mediating energy transfer between the stellar wind and the planetary magnetosphere.

3.4 Magnetotail current sheet as a function of stellar wind properties

While previous sections characterize the morphology and internal properties of Alfvén wings, we now investigate the global response of the magnetotail to combined changes in stellar wind forcing–a linear scaling between the night-side magnetotail current sheet length (L_{cs}) and the dimensionless composite forcing parameter

$$\widetilde{\Pi} = \frac{(v_{sw}/v_0)^2}{(B_{sw}/B_0)}, \tag{10}$$

where $v_0 = 350\,\mathrm{km\,s^{-1}}$ and $B_0 = 4.814 \times 10^{-4}\,\mathrm{G} = 48.14\,\mathrm{nT}$ are the reference (code) units of stellar-wind speed and magnetic field, respectively. This choice is physically motivated by magnetotail current-sheet-length scalings in which the current-sheet length increases with increasing stellar wind dynamic pressure and decreases with increasing interplanetary magnetic field strength (Gupta et al., 2023). The ratio between the dynamic-pressure driving of the stellar wind (proportional to $(v_{sw}/v_0)^2$) and the magnetic confinement exerted by the stellar wind (proportional to (B_{sw}/B_0)) as shown by Equation 10, effectively measures the relative importance of plasma kinetic pressure to the confining stellar-wind magnetic field strength.

Figure 4 shows the night-side magnetotail current sheet length as a function of the dimensionless parameter $\widetilde{\Pi}$. The simulated data points are well described by a linear relation for all three planetary dipole strengths, with coefficients of determination R^2 = 0.985, 0.946, and 0.861 for $B_p = 0.5\,B_e$, B_e and $2B_e$ respectively, confirming the robustness of the scaling. This linearity holds across a wide range of M_A regimes, suggesting that the stretching of the magnetotail behave predictably in response to the kinetic driving and magnetic tension. For all the cases, while the linear trend is consistent, the slope and intercept are determined by the planet's intrinsic magnetic field. The blue ($0.5B_e$), green ($1.0B_e$), and red ($2.0B_e$) curves show that for any given stellar wind condition, a stronger planetary dipole consistently maintains a longer current sheet.

This behavior indicates that stronger wind driving relative to the ambient stellar wind magnetic field is associated with a more extended magnetotail current sheet, whereas stronger B_{sw} at fixed v_{sw} is associated with a more compact tail. Within the range of parameters explored, this provides an empirical scaling that links upstream stellar wind conditions to the size of the magnetotail current sheet. The smaller slope for $B_p = 2\,B_e$ compared to $0.5\,B_e$ and B_e) indicates that, for a strongly magnetized planet, a given increase in $\widetilde{\Pi}$ produces less elongation of the current sheet. The scaling remains valid across the full range of upstream conditions explored, all of which are super-Alfvénic ($M_A > 1$), while the wings themselves form in the locally sub-Alfvénic near-planet wake. This implies

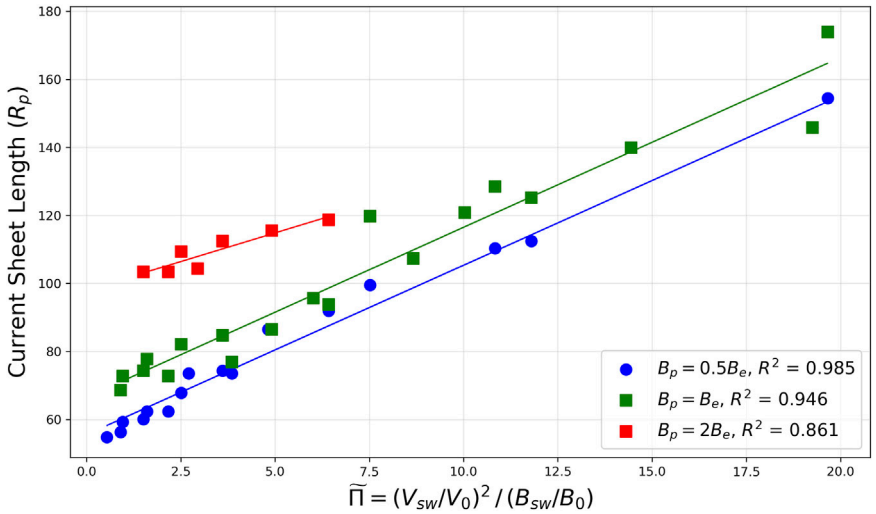


FIGURE 4
Night-side magnetotail current sheet length (L_{cs})as a function of the composite parameter $\widetilde{\Pi} = (v_{sw}/v_0)^2/(B_{sw}/B_0)$ for different planetary dipole field strengths where Alfvén wings form and finite current sheet lengths can be computed from simulations. Blue, green and red curves correspond to B_p = 0.5 B_e, B_e and 2 B_e respectively. Each curve aggregates simulation data across the stellar wind magnetic field strengths 10 nT, 30 nT and 50 nT.

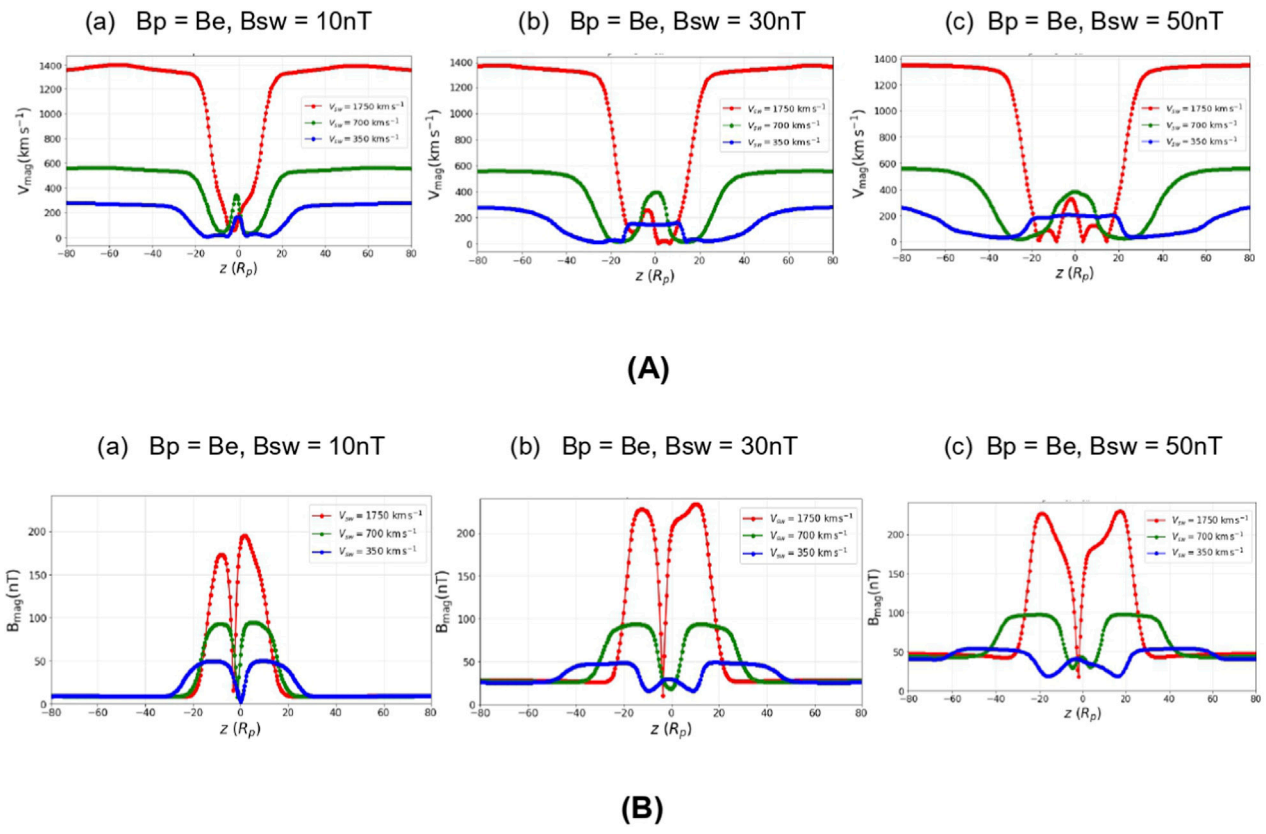


FIGURE 5
Plasma flow velocity and magnetic field strength inside the Alfvén wings for $B_p = B_e$ with varying stellar wind conditions. Panel **(A)** shows the flow velocity magnitude and panel **(B)** shows the magnetic field magnitude inside the wings. Blue, green and red curves correspond to stellar wind speeds of v_0, 2 v_0, and 5 v_0 respectively. In each panel, sub-panels (a-c) represent cases with stellar wind magnetic field strengths of 10 nT, 30 nT and 50 nT respectively. As expected, magnetic field lines are clustered inside the night-side Alfvén wings leading to magnetic field accumulation while the plasma flow significantly decreases inside the wings in the magnetotail region.

that the dimensionless parameter $\widetilde{\Pi}$ robustly describes magnetotail stretching across diverse star - planet systems.

4 Conclusion

The diversity of star-planet interactions that occur in the cosmos influence the dynamics of different planetary systems. In this work, we have explored several such (exo)planetary systems by carrying out a vast parameter-space study using 3D global magnetohydrodynamic (MHD) simulations–incorporating variations in stellar wind speed (v_{sw}), stellar magnetic field (B_{sw}), and planetary magnetic field (B_p) strengths. The first two parameters essentially represent the stellar wind forcing, while the last one characterizes the planetary magnetosphere. Variations in the above parameters influence the steady-state planetary environment and topology, especially the day-side magnetopause and the night-side Alfvén wings along with the associated magnetotail current sheets. By investigating a wide range of upstream conditions our parameter-space study–comprising ninety simulations–aims to illuminate the star-planet interaction physics at play and the consequent magnetospheric response.

The Alfvén wings emerge prominently when the local conditions become sub-Alfvénic and show an inverse scaling of the wing opening angle with stellar wind speed–lower wind speeds lead to broad, open wings, while higher speeds yield narrow, elongated structures. This morphological evolution reflects that increasing Alfvén Mach number compresses the wings to a more collimated structure along the flow direction, when the stellar wind magnetic field is increased keeping other parameters fixed, it tends to pull the wings apart resulting in a larger wing opening angle. A stronger planetary field, on the other hand, opposes the Lorentz force of the stellar wind and tends to close the wings down by bringing them closer to the ecliptic plane. The relative strength of these three parameters is, therefore, responsible for the steady-state morphology of the wings and the planetary environment. We further validate the simulated Alfvén wing opening angles against the analytical prediction of Neubauer (1980) with slight deviations arising from finite magnetospheric size.

Our analysis also reveals an inverse relationship between the subsolar magnetopause stand-off distance and the night-side magnetotail current sheet length for different values of the stellar wind speed. This trend can be explained using pressure balance–as the wind speed is increased, the ram pressure increases, which gradually compresses the day-side magnetosphere and stretches out the night-side magnetotail–resulting in a lower magnetopause stand-off distance and a longer magnetotail current sheet, respectively. A stronger stellar wind field compresses the magnetosphere, while a stronger planetary field expands the magnetosphere from both ends. We analyse the plasma flow inside the Alfvén wings. Within the wings, plasma flow decelerates while magnetic field strength enhances. The lateral extent of Alfvén wing increases with B_{sw} while with increasing stellar wind speed the wings become narrower. We also analyze the impact of the composite parameter $\widetilde{\Pi} = (v_{sw}/v_0)^2/(B_{sw}/B_0)$, a proxy for the ratio of dynamic-pressure driving to stellar magnetic confinement (associated with the magnetotail current-sheet length). The current sheet length scales approximately linearly with this parameter, suggesting a relation in which a stronger net kinetic driving relative to the magnetic confinement elongates the tail.

Our study presents a framework that relates stellar wind speed, stellar magnetic field, and planetary magnetic properties to the global evolution of magnetospheric morphology, Alfvén wing dynamics and magnetotail current sheets. The results indicate the relevance to solar system planets encountering extreme solar events, such as coronal mass ejections that may produce substantially reduced Alfvén Mach numbers when the local increase in magnetic-field strength and/or decrease in plasma density leads to an enhanced Alfvén speed relative to the flow speed, potentially creating conditions favorable for Alfvén-wing formation. The study is also relevant to (exo)planets orbiting active stars where sub-Alfvénic conditions prevail routinely. Our study is relevant for understanding how sub- and super-Alfvénic wind regimes influence the magnetospheric topology in both solar and extrasolar environments. By establishing qualitative scalings for wing morphology, tail structure, and plasma properties, our simulations provide a foundation for interpreting the observations of Alfvén wing structures and associated magnetospheric characteristics. We expect that these insights will motivate and inform future exploration of star-planet interactions in diverse astrophysical contexts.

Data availability statement

The raw data supporting the conclusions of this article will be made available by the authors, on reasonable request.

Author contributions

SG: Formal Analysis, Investigation, Methodology, Validation, Visualization, Writing – original draft, Writing – review and editing. AB: Conceptualization, Validation, Writing – review and editing. DN: Conceptualization, Resources, Supervision, Validation, Writing – review and editing.

Funding

The author(s) declared that financial support was received for this work and/or its publication. This work was supported through the computational facilities of the Center of Excellence in Space Sciences India, Indian Institute of Science Education and Research Kolkata. The article processing charge was waived by Frontiers.

Acknowledgments

The development of the Star - Planet Interaction module (CESSI-SPIM) and the simulations were carried out at the Center of Excellence in Space Sciences India (CESSI), supported by IISER Kolkata, Ministry of Education, Government of India. We gratefully acknowledge the Santimay and Sunanda Basu Foundation for enabling the computational infrastructure used in this study. SG acknowledges Dr. Jagannath Nayak, Director CHESS, and

Saumendra Nath Datta, Technology Director at CHESS, for the necessary approval and encouragement to continue her PhD research work at CESSI.

Conflict of interest

The author(s) declared that this work was conducted in the absence of any commercial or financial relationships that could be construed as a potential conflict of interest.

Generative AI statement

The author(s) declared that generative AI was not used in the creation of this manuscript.

Any alternative text (alt text) provided alongside figures in this article has been generated by Frontiers with the support of artificial intelligence and reasonable efforts have been made to ensure accuracy, including review by the authors wherever possible. If you identify any issues, please contact us.

Publisher's note

All claims expressed in this article are solely those of the authors and do not necessarily represent those of their affiliated organizations, or those of the publisher, the editors and the reviewers. Any product that may be evaluated in this article, or claim that may be made by its manufacturer, is not guaranteed or endorsed by the publisher.

References

Airapetian, V. S., Barnes, R., Cohen, O., Collinson, G. A., Danchi, W. C., Dong, C. F., et al. (2020). Impact of space weather on climate and habitability of terrestrial-type exoplanets. *Int. J. Astrobiol.* 19, 136–194. doi: 10.1017/S1473550419000132

Arridge, C., McAndrews, H., Jackman, C., Forsyth, C., Walsh, A., Sittler, E., et al. (2009). Plasma electrons in saturn's magnetotail: structure, distribution and energisation. *Planet. Space Sci.* 57, 2032–2047. doi: 10.1016/j.pss.2009.09.007

Basak, A., and Nandy, D. (2021). Modelling the imposed magnetospheres of mars-like exoplanets: star–planet interactions and atmospheric losses. *Mon. Notices R. Astronomical Soc.* 502, 3569–3581. doi: 10.1093/mnras/stab225

Beedle, J. M. H., Chen, L.-J., Shuster, J. R., Gurram, H., Gershman, D. J., Chen, Y., et al. (2024). Field-aligned current structures during the terrestrial magnetosphere's transformation into alfvén wings and recovery. *Geophys. Res. Lett.* 51, e2024GL108839. doi: 10.1029/2024GL108839

Belenkaya, E., Alexeev, I., and Kalegaev, V. (2024). Modeling of the exoplanet HAT-P-11b magnetosphere. *Astron. Rep.* 68, 39–47. doi: 10.1134/S1063772924700045

Belenkaya, E. (2025). Magnetic exoplanets in the subalvenic stellar wind: collimators of the interplanetary magnetic field. *Sol. Syst. Res.* 59, 40. doi: 10.1134/s0038094624601737

Belenkaya, E. S., Alexeev, I. I., and Blokhina, M. S. (2022). Modeling of magnetospheres of terrestrial exoplanets in the habitable zone around g-type stars. *Universe* 8, 231. doi: 10.3390/universe8040231

Bowers, C. F., Jackman, C. M., Jia, X., Hadid, L. Z., Sun, W., Hayes, L. A., et al. (2025). Mercury's altered magnetosphere during a sub-alfvénic icme event: messenger observations and inferred asymmetric alfvén wing formation from global mhd simulations. *J. Geophys. Res. Space Phys.* 130, e2025JA034248. doi: 10.1029/2025JA034248

Burkholder, B. L., Chen, L.-J., Sarantos, M., Gershman, D. J., Argall, M. R., Chen, Y., et al. (2024). Global magnetic reconnection during sustained sub-alfvénic solar wind driving. *Geophys. Res. Lett.* 51, e2024GL108311. doi: 10.1029/2024GL108311

Carolan, S., Vidotto, A. A., Loesch, C., and Coogan, P. (2019). The evolution of earth's magnetosphere during the solar main sequence. *Monthly Notices of the Royal Astronomical Society* 489, 5784–5801. doi: 10.1093/mnras/stz2422

Chané, E., Saur, J., Neubauer, F. M., Raeder, J., and Poedts, S. (2012). Observational evidence of Alfvén wings at the Earth. *J. Geophys. Res. Space Phys.* 117, A09217. doi: 10.1029/2012JA017628

Chen, L.-J., Gershman, D., Burkholder, B., Chen, Y., Sarantos, M., Jian, L., et al. (2024). Earth's alfvén wings driven by the April 2023 coronal mass ejection. *Geophys. Res. Lett.* 51, e2024GL108894. doi: 10.1029/2024GL108894

Cohen, O., Drake, J. J., Glocer, A., Garraffo, C., Poppenhaeger, K., Bell, J. M., et al. (2014). Magnetospheric structure and atmospheric joule heating of habitable planets orbiting m-dwarf stars. *Astrophysical J.* 790, 57. doi: 10.1088/0004-637X/790/1/57

Corso, N. J., and Lai, D. (2026). Simulations of a conducting sphere moving through magnetized plasma: alfvén wings, slow magnetosonic wings, and drag force. *Astrophysical J.* 1002, 1. doi: 10.3847/1538-4357/ae5817

Das, S. B., Basak, A., Nandy, D., and Vaidya, B. (2019). Modeling star–planet interactions in far-out planetary and exoplanetary systems. *Astrophysical J.* 877, 80. doi: 10.3847/1538-4357/ab18ad

Drell, S. D., Foley, H. M., and Ruderman, M. A. (1965). Drag and propulsion of large satellites in the ionosphere: an alfvén propulsion engine in space. *J. Geophys. Res. (1896-1977)* 70, 3131–3145. doi: 10.1029/JZ070i013p03131

Dungey, J. W. (1961). Interplanetary magnetic field and the auroral zones. *Phys. Rev. Lett.* 6, 47–48. doi: 10.1103/PhysRevLett.6.47

Ganushkina, N. Y., Liemohn, M. W., and Dubyagin, S. (2018). Current systems in the earth's magnetosphere. *Rev. Geophys.* 56, 309–332. doi: 10.1002/2017RG000590

Garraffo, C., Drake, J. J., Cohen, O., Alvarado-Gómez, J. D., and Moschou, S. P. (2017). The threatening magnetic and plasma environment of the trappist-1 planets. *Astrophysical J. Lett.* 843, L33. doi: 10.3847/2041-8213/aa79ed

Gupta, S., Basak, A., and Nandy, D. (2023). Impact of changing stellar and planetary magnetic fields on (exo)planetary environments and atmospheric mass loss. *Astrophysical J.* 953, 70. doi: 10.3847/1538-4357/acd93b

Gurram, H., Shuster, J. R., Chen, L.-J., Hasegawa, H., Denton, R. E., Burkholder, B. L., et al. (2025). Earth's alfvén wings: unveiling dynamic variations of field-line topologies with electron distributions. *Geophys. Res. Lett.* 52, e2024GL111931. doi: 10.1029/2024GL111931

Jia, X., Walker, R. J., Kivelson, M. G., Khurana, K. K., and Linker, J. A. (2008). Three-dimensional mhd simulations of ganymede's magnetosphere. *J. Geophys. Res. Space Phys.* 113, A06212. doi: 10.1029/2007JA012748

Kivelson, M. G., Khurana, K. K., Coroniti, F. V., Joy, S., Russell, C. T., Walker, R. J., et al. (1997). The magnetic field and magnetosphere of ganymede. *Geophys. Res. Lett.* 24, 2155–2158. doi: 10.1029/97GL02201

Komar, C. M., Cassak, P. A., Dorelli, J. C., Glocer, A., and Kuznetsova, M. M. (2013). Tracing magnetic separators and their dependence on imf clock angle in global magnetospheric simulations. *J. Geophys. Res. Space Phys.* 118, 4998–5007. doi: 10.1002/jgra.50479

Lammer, H., Lichtenegger, H. I., Kulikov, Y. N., Grießmeier, J.-M., Terada, N., Erkaev, N. V., et al. (2007). Coronal mass ejection (cme) activity of low mass m stars as an important factor for the habitability of terrestrial exoplanets. ii. Cme-induced ion pick up of earth-like exoplanets in close-in habitable zones. *Astrobiology* 7, 185–207. doi: 10.1089/ast.2006.0128

Lockwood, M. (1995). Large-scale fields and flows in the magnetosphere-ionosphere system. *Surv. Geophys.* 16, 389–441. doi: 10.1007/bf01044574

Lugaz, N., Farrugia, C. J., Huang, C.-L., Winslow, R. M., Spence, H. E., and Schwadron, N. A. (2016). Earth's magnetosphere and outer radiation belt under sub-alfvénic solar wind. *Nat. Commun.* 7, 13001. doi: 10.1038/ncomms13001

Mignone, A., Bodo, G., Massaglia, S., Matsakos, T., Tesileanu, O., Zanni, C., et al. (2007). PLUTO: a numerical code for computational astrophysics. *Astrophysical J. Suppl. Ser.* 170, 228–242. doi: 10.1086/513316

Milan, S. E., Carter, J. A., Sangha, H., Bower, G. E., and Anderson, B. J. (2021). Magnetospheric flux throughput in the dungey cycle: identification of convection state during 2010. *J. Geophys. Res. Space Phys.* 126, e2020JA028437. doi: 10.1029/2020JA028437

Nandy, D., and Martens, P. (2007). Space climate and the solar–stellar connection: what can we learn from the stars about long-term solar variability? *Adv. Space Res.* 40, 891–898. doi: 10.1016/j.asr.2007.01.079

Neubauer, F. (1980). Nonlinear standing alfvén wave current system at io: theory. *J. Geophys. Res. Space Phys.* 85, 1171–1178. doi: 10.1029/JA085iA03p01171

Nichols, J. D., and Milan, S. E. (2016). Stellar wind–magnetosphere interaction at exoplanets: computations of auroral radio powers. *Mon. Notices R. Astronomical Soc.* 461, 2353–2366. doi: 10.1093/mnras/stw1430

Pérez-Torres, M., Gómez, J. F., Ortiz, J. L., Leto, P., Anglada, G., Gómez, J. L., et al. (2021). Monitoring the radio emission of proxima centauri. *A&A* 645, A77. doi: 10.1051/0004-6361/202039052

Pineda, J. S., and Villadsen, J. (2023). Coherent radio bursts from known m-dwarf planet-host yz ceti. *Nat. Astron.* 7, 569–578. doi: 10.1038/s41550-023-01914-0

Presa, A., Driessen, F. A., and Vidotto, A. A. (2024). Atmospheric escape in hot jupiters under sub-alfvénic interactions. *Mon. Notices R. Astronomical Soc.* 534, 3622–3636. doi: 10.1093/mnras/stae2325

Raeder, J. (1999). Modeling the magnetosphere for northward interplanetary magnetic field: effects of electrical resistivity. *J. Geophys. Res. Space Phys.* 104, 17357–17367. doi: 10.1029/1999JA900159

Ridley, A. J. (2007). Alfvén wings at earth's magnetosphere under strong interplanetary magnetic fields. *Ann. Geophys.* 25, 533–542. doi: 10.5194/angeo-25-533-2007

Roy, S., and Nandy, D. (2023). A time-efficient, data-driven modeling approach for predicting the geomagnetic impact of coronal mass ejections. *Astrophysical J. Lett.* 950, L11. doi: 10.3847/2041-8213/acd77c

Sarantos, M., and Slavin, J. A. (2009). On the possible formation of alfvén wings at mercury during encounters with coronal mass ejections. *Geophys. Res. Lett.* 36, L04107. doi: 10.1029/2008GL036747

Saur, J., Grambusch, T., Duling, S., Neubauer, F. M., and Simon, S. (2013). Magnetic energy fluxes in sub-alfvénic planet star and moon planet interactions. *A&A* 552, A119. doi: 10.1051/0004-6361/201118179

See, V., Jardine, M., Vidotto, A. A., Petit, P., Marsden, S. C., Jeffers, S. V., et al. (2014). The effects of stellar winds on the magnetospheres and potential habitability of exoplanets ★. *A&A* 570, A99. doi: 10.1051/0004-6361/201424323

Sergeev, V. A., Angelopoulos, V., and Nakamura, R. (2012). Recent advances in understanding substorm dynamics. *Geophys. Res. Lett.* 39, L05101. doi: 10.1029/2012GL050859

Slavin, J. A., Smith, E. J., Spreiter, J. R., and Stahara, S. S. (1985). Solar wind flow about the outer planets: gas dynamic modeling of the jupiter and saturn bow shocks. *J. Geophys. Res. Space Phys.* 90, 6275–6286. doi: 10.1029/JA090iA07p06275

Szalay, J. R., Bagenal, F., Allegrini, F., Bonfond, B., Clark, G., Connerney, J. E. P., et al. (2020). Proton acceleration by io's alfvénic interaction. *J. Geophys. Res. Space Phys.* 125, e2019JA027314. doi: 10.1029/2019JA027314

Varela, J., Brun, A. S., Strugarek, A., Réville, V., Zarka, P., and Pantellini, F. (2022). Mhd study of the planetary magnetospheric response during extreme solar wind conditions: earth and exoplanet magnetospheres applications. *A&A* 659, A10. doi: 10.1051/0004-6361/202141181

Vidotto, A. A., and Cleary, A. (2020). Stellar wind effects on the atmospheres of close-in giants: a possible reduction in escape instead of increased erosion. *Mon. Notices R. Astronomical Soc.* 494, 2417–2428. doi: 10.1093/mnras/staa852

Vidotto, A. A., Gregory, S. G., Jardine, M., Donati, J. F., Petit, P., Morin, J., et al. (2014). Stellar magnetism: empirical trends with age and rotation. *Mon. Notices R. Astronomical Soc.* 441, 2361–2374. doi: 10.1093/mnras/stu728

Zank, G. P., le Roux, J. A., Webb, G. M., Dosch, A., and Khabarova, O. (2014). Particle acceleration via reconnection processes in the supersonic solar wind. *Astrophysical J.* 797, 28. doi: 10.1088/0004-637X/797/1/28